

# Testing the relativistic Doppler boost hypothesis for supermassive binary black holes candidates via broad emission line profiles

Zihao Song<sup>1,2</sup>, Junqiang Ge<sup>1</sup>, Youjun Lu<sup>1,2,†</sup>, and Xiang Ji<sup>1,2</sup>

<sup>1</sup>National Astronomical Observatories, Chinese Academy of Sciences, 20A Datun Road, Beijing, 100101, China; [lyyj@nao.cas.cn](mailto:lyyj@nao.cas.cn)

<sup>2</sup>School of Astronomy and Space Science, University of Chinese Academy of Sciences, No. 19A Yuquan Road, Beijing, 100049, China

4 February 2022

## ABSTRACT

Optical periodicity QSOs found by transient surveys are suggested to be sub-parsec supermassive binary black holes (BBHs). An intriguing interpretation for the periodicity of some of those QSOs is that the continuum is radiated from the accretion disk associated with the BBH secondary component and modulated by the periodical rotation of the secondary via Doppler-boost effect. Close to edge-on orbital orientation can lead to more significant Doppler-boost effect and thus are preferred for these systems, which is distinct from those normal type-1 QSOs with more or less face-on orientations. Therefore, the profiles of broad lines emitted from these Doppler-modulated systems may be significantly different from other systems that are not Doppler-modulated. We investigate the properties of the broad emission lines of optical-periodicity QSOs, including both a sample of QSOs that can be interpreted by the Doppler-modulated effects and a sample that cannot. We find that there is no obvious difference in the profiles and other properties of various (stacked) broad emission lines of these two samples, though a simple broad line region model would suggest significant differences. Our finding raises a challenge to the Doppler boost hypothesis for some of those BBHs candidates with optical periodicity.

**Key words:** black hole physics—line: profiles—galaxies: active—galaxies: quasars: supermassive black holes

## 1 INTRODUCTION

Supermassive binary black holes (SMBBHs) have long been anticipated to exist in centers of many galaxies as the natural products of hierarchical galaxy mergers (e.g., Begelman et al. 1980; Yu 2002) because most galaxies host a massive black hole (MBH) in their centers (e.g., Magorrian et al. 1998; Tremaine et al. 2002; Kormendy & Ho 2013). Searching for sub-parsec SMBBHs has become a hot topic in recent years, and a number of candidates have been found according to various plausible SMBBH signatures, including particular line features, such as double-peaked/asymmetric line profile or offset lines (e.g., Tsalmantza et al. 2011; Eracleous et al. 2012; Ju et al. 2013; Liu et al. 2014; Guo et al. 2019), optical-UV flux deficit (e.g., Yan et al. 2015; Zheng et al. 2016), and periodical variation of light curves (e.g., Graham et al. 2015a,b; Charisi et al. 2016, 2018; Li et al. 2019). However, it is still difficult to confirm that any of these candidates is really a sub-parsec SMBBH system.

Among those candidates, more than 100 are the optical periodicity QSOs (typically with period about 1 to a

few years) found through transient surveys (e.g., Catalina Real-time Transient Survey, Palomar Transient Factory, and Rapid Response System (Pan-STARRS)), of which some were suggested to be due to orbital modulated accretion rate variation (e.g., Graham et al. 2015a; Charisi et al. 2016; Liu et al. 2019) or relativistic Doppler boosted continuum radiation from active SMBBH systems. The most intriguing example is PG 1302-102, of which the optical-UV continuum variation appears to be consistent with the Doppler boosting of the continuum radiation from the disk associated with the secondary MBH (e.g., D’Orazio et al. 2015; Xin et al. 2019). Charisi et al. (2018) have further investigated the viability of Doppler boost interpretation for a sample of those SMBBH candidates with optical periodicity by using their optical-UV continua, the steeper the UV continua, the more significant the Doppler boost effect. They found that about one-third of them can be interpreted as the Doppler-modulated SMBBHs while others cannot, although these targets may be still contaminated by normal QSOs (with a maximum fraction of 37% in the FUV band) due to their color-dependent variability.

Apparently the Doppler boost effect is also dependent on the orientation of orbital plane relative to the line of sight (LOS), and the effects for those systems with close to edge-on orbital orientation are much more significant than that for face-on ones, which require higher rotating velocities to present similar Doppler boost effect as the edge-on cases. Therefore, the orbital orientation for those systems that can be interpreted by the Doppler boost effect may be more likely to have close to edge-on orbital orientations. According to [Graham et al. \(2015a\)](#), for example, the orbital inclination of PG 1302-102, defined as the angle between the disk normal and the LOS, requires to be  $\gtrsim 60^\circ$  if its optical periodicity is explained by the Doppler boost effect. However, normal QSOs or those QSOs with optical-periodicity but not due to the Doppler boost are supposed to have more face-on oriented disk according to the standard AGN unification model (e.g., [Antonucci 1993](#); [Krolik 1999](#)). Assuming the orbital plane is aligned with the disk, then the profiles of broad lines of the Doppler-modulated systems are expected to be systematically different from that of those systems with insignificant Doppler boost effects due to the possible systematic differences in the disk orientations, since broad line regions (BLRs) are generally flattened and not spherical ([Pancoast et al. 2012, 2014a,b](#); [Williams et al. 2018](#)). If the BLR is not aligned with the BBH orbital plane or they are significantly mis-aligned, the systematic difference may become weaker.

In this paper, we investigate the properties, especially profiles, of the broad emission lines of those optical-periodicity QSOs, and check whether there are systematic differences in the broad lines emitted from those BBH candidates that can be interpreted by the Doppler-modulated effects and those that cannot. The paper is organized as follows. In Section 2, we introduce the optical-periodicity QSO samples, data analysis of spectroscopic data adopted from [Charisi et al. \(2018\)](#), and a BLR model to fit broad line profile. In Section 3, we present main results on the line properties of individual sample objects and the stacked line profiles for both the sample that can be interpreted by the Doppler boost effect and that cannot, then we test the Doppler boost hypothesis, by comparing the expected stacked broad line profile, obtained for the proposed Doppler boost sample objects via the simple BLR model, with the observational one. Conclusions are summarized in Section 4.

## 2 SAMPLE, DATA ANALYSIS, AND A SIMPLE BLR MODEL FOR LINE PROFILE

### 2.1 Sample

[Charisi et al. \(2018\)](#) collected a sample of BBH candidates via optical periodic variations, including 21 objects of which the periodicity was proposed to be due to relativistic Doppler boost (DB; here after denoted as DB objects), and 47 objects of which the periodicity is not due to relativistic Doppler boost (hereafter denoted as non-DB objects). By cross-matching those objects with the SDSS spectral catalog DR13 ([Albaret et al. 2017](#)), we find that all the 21 DB objects and 40 out of the 47 non-DB objects have SDSS spectra. Hereafter we take those 21 DB objects as the DB sample and those 40 non-DB objects as the non-DB sample.

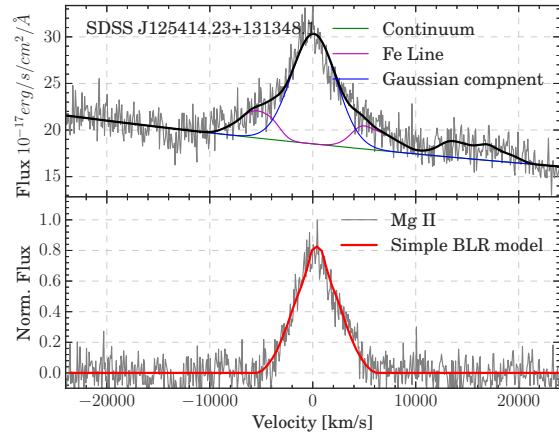


**Figure 1.** Examples of the spectral fitting (top panel) and the model fitting to the line profile of Mg II (bottom panel; for object SDSS J125414.23+131348.1). In the top panel, the observed spectrum (grey curve) is fitted by the combination of three components, i.e., a power-law continuum (green), a Gaussian Mg II broad line (blue), and multiple lines from Fe II templates by [Sigut et al. \(2004\)](#) described by Gaussian profiles with the same velocity dispersion (magenta). The best fit is shown by the black curve in the top panel. In the bottom panel, the grey curve shows the Mg II profile obtained by subtracting the best-fit continuum and Fe II lines from the observed spectrum. The red line represents the best-fit Mg II profile to the grey curve obtained from the simple BLR model introduced in Section 2.3.

### 2.2 Data analysis

For the DB and non-DB samples, we can identify broad emission lines like C III], C IV, Mg II, and others from their SDSS spectra. The numbers of these BBH candidates that have Mg II, C III], and C IV lines in their SDSS spectra are among the top three, hence we take them for following analysis. We adopt a model with three components to fit each observed spectrum, i.e., a power-law for continuum, a Gaussian profile for each broad line, and multiple lines from Fe II templates ([Sigut & Pradhan 2003](#); [Sigut et al. 2004](#)) described by Gaussian profiles with the same velocity dispersion (which can be different from that for the broad line). Fe II lines are considered here as they contaminate the above three lines (especially Mg II) significantly. The wavelength windows in the rest frame for the fittings to each broad line are 1450-1650, 1800-2000, and 2700-3000 Å, respectively, and the windows for Fe II lines are 1450-1530, 1570-1650, 1800-1880, 1940-2000, 2700-2770, and 2830-3000 Å. A broad emission line, either C III], C IV, or Mg II is confirmed if the best fit gives an FWHM  $> 1000$  km/s and a peak flux  $> 3\sigma$  significance. Figure 1 shows an example for such a model fitting to Mg II line of an object SDSS J125414.23+131348.1 (top panel). The total numbers of those objects that have confirmed broad emission line C III], C IV, and Mg II in each sample are listed in Table 1, respectively. As seen from Table 1, most sample objects have confirmed Mg II, while only a small fraction (or  $\lesssim 50\%$ ) of the sample objects have confirmed C IV or C III] lines.

We analyze these three broad emission lines in the following ways in order to investigate the properties of the DB

**Table 1.** Number of BBH candidates that have different broad lines in their SDSS spectra

sample	C IV	C III]	Mg II
DB	7	12	21
non-DB	7	13	36

and non-DB samples. First, we stack the observed profiles of each line together for each sample, in which the integrated flux of each line is normalized to 1 before stacking. In this way, we may find whether there is a systematic difference between the mean line properties of the two samples. Second, we compare the FWHM distributions of each broad line resulting from the above model fittings to the objects in both samples. If the DB and non-DB samples are correctly classified based on the relativistic DB, then this DB effect should be reflected by the difference between the stacked line profiles of the DB sample and that of the non-DB sample, as well as the differences between the FWHM distributions of the lines for objects in the DB sample and that in the non-DB sample, provided that the geometry of BLR is flattened and the DB objects are preferably viewed at a directly close to edge-on.

Beside the mean profile and the FWHM distribution, another important quantity to indicate the difference is the inclination angle of the BLR, which can not be derived without BLR modeling. To have a further understanding on line properties for objects in those two samples, below we introduce a simple BLR model in order to give a rough estimation of the inclination angle for each object.

### 2.3 A simple model for the broad line fitting

The broad emission line profiles are determined by the BLR geometry, kinematics, and structures. We assume that BLR is composed of a large number of clouds/clumps, rotating around the central supermassive black hole(s) on circular orbits due to gravity. We assume that the number density distribution of the BLR clouds/clumps is only a function of radius, and it is cut at an inner radius of  $R_{\text{in}}$ . The BLR may be also flattened. Based on these simple assumptions, the line profile can be simply estimated as (Blumenthal & Mathews 1975, 1976)

$$F(\lambda) \simeq \int_{R_{\text{in}}}^{R_{\text{out}}} \int_{\theta_1}^{\theta_2} \int_0^{2\pi} n_c(r) j_c(r) \delta \left[ \lambda - \lambda_0 \left( 1 + \frac{v_{\parallel}}{c} \right) \right] \times r^2 \sin \theta dr d\theta d\phi, \quad (1)$$

where  $\lambda_0$  is the center of a line,  $n_c(r)$  the number density distribution of clouds,  $j_c(r)$  the emissivity,  $v_{\parallel}$  is the projected velocity of a cloud along the LOS,  $\theta_1$  and  $\theta_2$  defining the flattening of the BLR. In our calculation,  $j_c$  is set to be constant.

The semi-major axis of a BBH system with a total mass of  $M_{\bullet\bullet}$  and a period of  $P_{\text{orb}}$  can be roughly estimated as

$$a_{\text{BBH}} = 6.75 \left( \frac{M_{\bullet\bullet}}{10^8 M_{\odot}} \right)^{1/3} \left( \frac{P_{\text{orb}}}{1460 \text{ day}} \right)^{2/3} \text{ lt-days}. \quad (2)$$

All the sub-parsec BBH candidates in our sample have periodic variations on timescales around a few years, which are

taken as the orbital periods of the binary systems. Adopting the above equation, we can thus estimate the semi-major axis for each BBH candidate in our sample by adopting those values for  $M_{\bullet\bullet}$  and  $P_{\text{orb}}$  given in Graham et al. (2015b) and Charisi et al. (2016).

For an active MBH, the BLR size can be inferred from its optical luminosity by using the empirical relationship between BLR size and optical luminosity given by (Bentz et al. 2013; Lu et al. 2016), i.e.,

$$\log(R_{\text{BLR}}^L / \text{lt-day}) \simeq 1.527 + 0.533 \log \left[ \frac{\lambda L_{\lambda}(5100 \text{ \AA})}{10^{44} \text{ erg s}^{-1}} \right] \quad (3)$$

with a scatter of  $\sim 0.13 - 0.2$  dex (see also Kaspi et al. 2000, 2007). This tight relationship is basically a result of the photon-ionization nature of broad emission lines (Peterson 1997). For this reason, the BLR size of a BBH system can be similarly estimated if BLR is far away from the BBH, although the difference in the potential of a BBH system from that of a single black hole system may have some effect. We therefore adopt Equation (3) to estimate the BLR size for each BBH candidate.

We find that  $R_{\text{BLR}}^L$  of those BBH systems are substantially larger than their semi-major axes according to above calculations. The ratio  $R_{\text{BLR}}^L / a_{\text{BBH}}$  ranges from about 6 to 136 for the BBH candidates in our sample, with a median value of 42. Therefore, it is safe to assume that those broad lines are emitted from regions rotating around but far away from the binary systems, i.e., a circum-binary BLR.

The BLR geometry and structure have been intensively studied in the past several decades and it becomes clear only recently. Pancoast et al. (2014a) find that the BLRs of a few AGNs are significantly flattened, with an opening angle of  $\sim 27^\circ - 49^\circ$ . Gravity Collaboration et al. (2018) make a breakthrough discovery on the BLR structure of 3C 273 by resolving its kinematics and find the half opening angle of the flattened BLR is about  $45^\circ$ , consistent with the results by Pancoast et al. (2014a). Therefore, we model the geometry of a BLR similar to that described in Section 2.4 of Pancoast et al. (2014a), and define it with six free parameters: the mean and inner radius of BLR ( $R_{\text{BLR}}, R_{\text{in}}$ ), radial shape parameter  $\beta$ , opening angle  $\theta_0$ , inclination angle  $i_{\text{BLR}}$ , and the central black hole mass  $M_{\text{BH}}$ .

For each broad emission line, we perform the Markov Chain Monte Carlo (MCMC) calculations by using the software package “emcee” (Foreman-Mackey et al. 2013) to derive the best fitting results of the above six parameters. The initial parameter setups are as follows. We allow  $R_{\text{BLR}}$  to vary from  $0.1 R_{\text{BLR}}^L$  to  $5 R_{\text{BLR}}^L$ .<sup>1</sup> For each  $R_{\text{BLR}}$ , we set the inner radius of the BLR as  $R_{\text{in}}$  in the range of  $[0, R_{\text{BLR}}]$ .

<sup>1</sup> Note that the estimated MBH mass for each object may depend on the assumption of the BLR geometry and others and thus biased from the true MBH mass by a factor of 3 or so (Krolik 2001). However, the line profile basically depends on the velocity field of the broad line clouds, which depends on  $\sqrt{M_{\bullet\bullet}/d_c}$  with  $d_c \sim R_{\text{BLR}}$  defined as the distance from a cloud to the mass center, if assuming circular orbits. Therefore, the uncertainties in the mass estimates can be absorbed into the uncertainties of  $R_{\text{BLR}}^L$ . For this reason, we assume  $R_{\text{BLR}}$  varies from  $0.1 R_{\text{BLR}}^L$  to  $5 R_{\text{BLR}}^L$  (by also considering the scatter in the estimates of  $R_{\text{BLR}}^L$  according to Eq. 3) and we do not separately consider the mass uncertainties in our simple model for fitting the broad line profile.

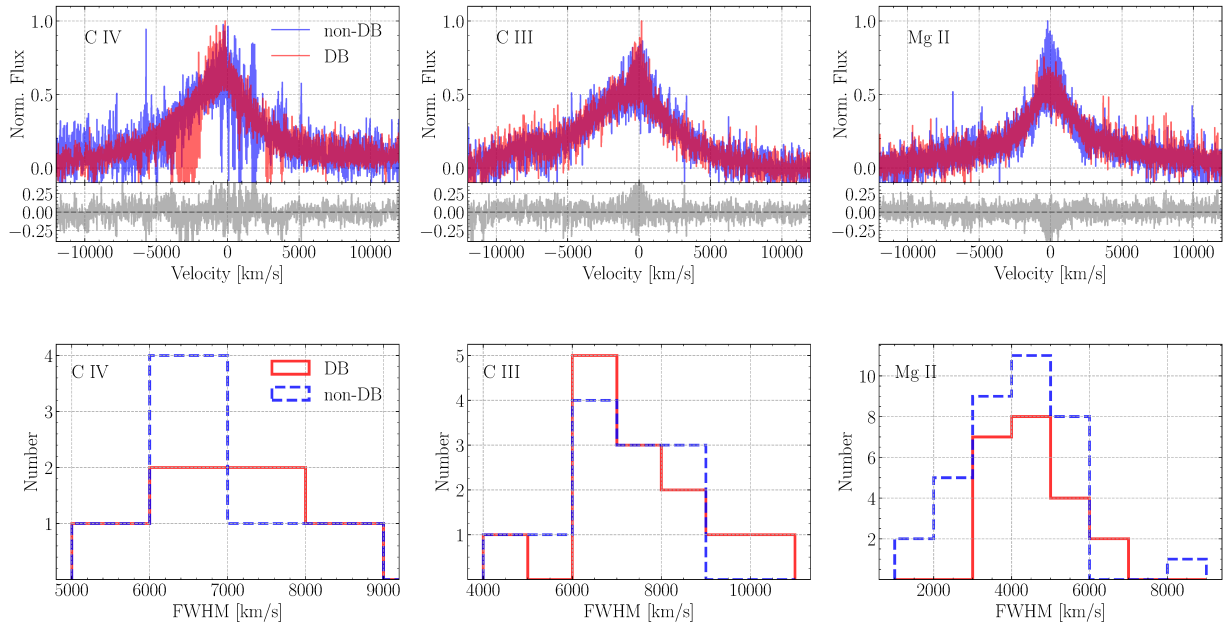


**Figure 2.** The stacked C IV+Fe II, C III+Fe II, and Mg II+Fe II broad lines (top panels from left to right) and the FWHM distributions for the C IV, C III, and Mg II broad lines among the objects in the DB sample and the non-DB sample (bottom panels from left to right), respectively. In each top (bottom) panel, red and blue curves (histograms) represent the results obtained for the DB and non-DB sample, respectively. In each of the three small panels right below the top panels, the grey curve shows the difference between the stacked line profile of the DB sample (red curve) and that of the non-DB sample (blue curve). This figure illustrates that there is no significant statistical difference between the profiles of the broad lines emitted from objects in the DB sample and those from objects in the non-DB sample.

The inclination angle ( $i_{\text{BLR}}$ ) is set to be in the range from  $0^\circ$  (face-on) to  $90^\circ$  (edge-on). The open angle varies in range of  $[0^\circ, 90^\circ]$ , and central black hole mass are in the range of  $[0.1M_\bullet, 5M_\bullet]$ . The bottom panel of Figure 1 shows an example of the fitting, in which the model profile (red line) matches the observed line profile well (with a reduced  $\chi^2_\nu \sim 1$ ).

### 3 RESULTS

We present our main results on stacked line profiles and fitting the broad line profiles via the simple BLR model introduced in Section 2.3.

#### 3.1 Stacked line profiles

Figure 2 shows the stacked C IV+Fe II (top-left panel), C III+Fe II (top-middle panel), and Mg II+Fe II (top-right panel) for the DB and non-DB samples, respectively, and also shows the FWHM distributions of those lines among the objects in each sample (from bottom left to right panels). In each top (bottom) panel, the blue and red curves (histograms) represent results obtained for the non-DB sample and DB sample, respectively. The difference between the two stacked profiles shown in each top panel is correspondingly shown in a small panel right below it, and it is fluctuating around 0 at different wavelengths. We also apply t-test to check whether the two FWHM distributions shown in each bottom panel are significantly different from each other, and

we obtain t-test p-values as 0.31 (C IV), 0.34 (C III), and 0.38 (Mg II), respectively, which suggest that the FWHM distribution of each line of the DB objects is statistically not different from that of the non-DB objects. This figure clearly demonstrates that the stacked profiles of each broad line obtained for the DB and non-DB samples are almost the same.

Under the Doppler hypothesis, however, we note here the stacked broad line profile for the proposed DB objects is expected to be different from that of non-DB objects as the proposed DB objects are supposed to be viewed preferentially at close to edge-on direction while the non-DB objects are not, if assuming that the non-DB and DB objects have the same BLR geometry and structure. This expectation seems to be in contradict with the observational results presented above. To further understand the observational results and its constraints on the Doppler boost hypothesis for some BBH candidates, we further adopt the simple BLR model to investigate the broad line properties of the DB and non-DB objects below.

#### 3.2 Line profile Modelling and Observational Constraints on the DB hypothesis

We apply the Python MCMC code “emcee” to constrain parameters of the simple BLR model introduced in Section 2.3, by fitting the Mg II broad line of each object in both the DB and non-DB samples. Here we only consider Mg II because it is identified in the SDSS spectra of most objects in our sample (Table 1), while other lines are only identified in



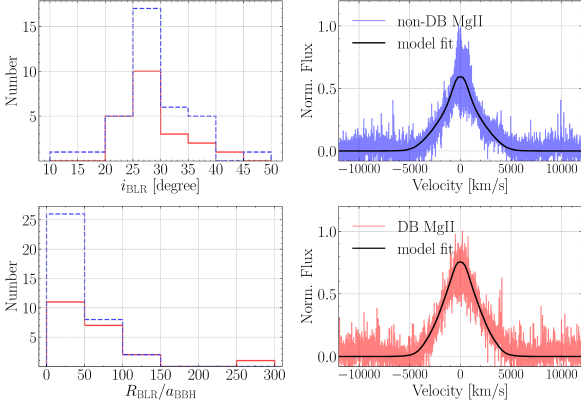


**Figure 3.** Top- and bottom-left panels show the distributions of the best-fit model parameters (assuming the simple BLR model introduced in Section 2.3), i.e., inclination angle  $i$  and BLR size  $R_{\text{BLR}}$  (in unit of  $a_{\text{BBH}}$ ), among the objects in the non-DB (blue histogram) and DB (red histogram) samples, respectively. Top- and bottom-right panels show the stacked line profiles for Mg II (by subtracting the best-fit continuum and Fe II lines) obtained for the non-DB (blue curve) and DB (red curve) samples, and also the stacked modelled line profile (black lines) by adding the best-fit Mg II profile of each object in the two samples, respectively.

the SDSS spectra of a small number of sample objects. By matching the observed line profile, we can derive the inclination angle and the BLR size of each BBH system.

Figure 3 shows the distributions of the model parameters [i.e., inclination angle  $i$  (top-left panel) and mean BLR size in unit of the BBH semi-major axis (bottom-left panel)] obtained from the simple BLR model, and the stacked profiles obtained from the best-fits to Mg II for the DB (bottom-right panel) and non-DB (top-right panel) objects, respectively. As seen from this figure, the inclination angles obtained from the model fittings to both DB and non-DB objects are mostly in the range from a few to  $\sim 45$  degree, which suggests that those sample objects are observed at orientations preferentially face-on. The best-fit BLR size is significantly larger than the semi-major axis for each BBH candidate ( $R_{\text{BLR}}/a_{\text{BBH}}$  in the range from 14 to 286), this again validates the assumption of circum-binary BLR made in Section 2.3. The stacked profiles obtained from the best-fits of Mg II lines (black lines in right panels) also match the observed profiles well for both the non-DB (top-right panel) and DB (bottom-right panel) samples.

The inclination angles for the proposed DB objects are expected to be systematically larger than those for the non-DB objects if the Doppler boost hypothesis is correct (Charisi et al. 2018), as DB objects are preferentially observed at close to edge-on orientations. Such an expected difference in inclination angles would lead to significant difference between the stacked broad line profiles of the DB objects and those of the non-DB objects. To check such line profile differences, we take the best-fits of BLRs for Mg II lines of those 36 non-DB objects as templates, and randomly choose 21 of them and replace the inclination angle for each of these 21 objects by a new one randomly selecting from  $\sin i$  over the range from  $\sin 45^\circ$  to  $\sin 90^\circ$  [see incli-

nation angle distribution (red histogram) in top-left panel]. These 21 objects are taken as the mock DB sample, of which the Mg II profiles can be calculated according to the simple BLR model and added together to form a stacked Mg II line profile that is expected for the proposed DB sample under the Doppler boost hypothesis. For each mocked profile, we add the flux error to it based on the observed flux error of each Mg II broad line by assuming that the flux uncertainty at each wavelength follow a normal distribution. The stacked profile is then obtained by stacking all the mocked profiles of QSOs in the mock DB sample, as shown by the red curve and the associated shaded region in the top-right panel of Figure 4. Obviously the expected stacked Mg II profile of the mock DB sample appears top-flat and has a weak double-peaked feature, different from that for the non-DB sample with a single peak, and it is also significantly broader than that for the non-DB sample. The detailed differences of stacked Mg II profiles between the mock DB sample and the non-DB sample are also shown in the bottom-right panel of Figure 4, which present significantly different valleys and summit from that shown in Figure 2 (see also differences in the FWHM distributions shown in bottom-left panel of Fig. 4). This expected stacked Mg II profile is significantly different from that obtained directly from observations for the DB sample classified in Charisi et al. (2018), which provides a robust evidence to disapprove the DB and non-DB sample classifications obtained under the Doppler boosting hypothesis in Charisi et al. (2018), assuming that the orbital plane is aligned with the disk for each target, and those DB objects and non-DB objects have similar BLR geometry and structures.

The DB QSOs maybe contaminated by those with color-dependent variability of 20% and 37% in the nUV and fUV bands, respectively, that mimic the Doppler boosting signatures (Charisi et al. 2018). In the DB sample, there are 7 QSOs identified by both the NUV and FUV bands, and 14 QSOs only by the NUV band. To clarify how the contaminated QSOs may affect our statistical analyses on the comparison of DB and non-DB samples, we perform Monte-Carlo simulations to construct a new DB sample by removing randomly selected 20% and 37% of the QSOs selected from the NUV and FUV bands in the DB sample, respectively. With the re-constructed DB sample, we perform the same analysis procedures as done to the DB sample above. By performing ten thousands of such simulations, we find that the stacked line profiles for those re-constructed samples are all similar to that of DB sample, without removing 20% and 37% sources (red curve in the bottom-right panel of Fig. 3), and no one is similar to the red curve shown in Figure 4. These simulations verify that although the DB sample is possibly contaminated by normal QSOs, the sample properties of the DB sample are still statistically robust and the possible contamination dose not affect our conclusion.

### 3.3 Orbital orientations of the DB sample

The above analyses are based on the assumption that the BBH orbital plane is aligned with disk, however, whether they are really aligned or not is still unclear. To figure out how this alignment or misalignment can affect our understanding on the DB sample, we try to explore more details on the orientations of the orbital plane and BLR as follows.

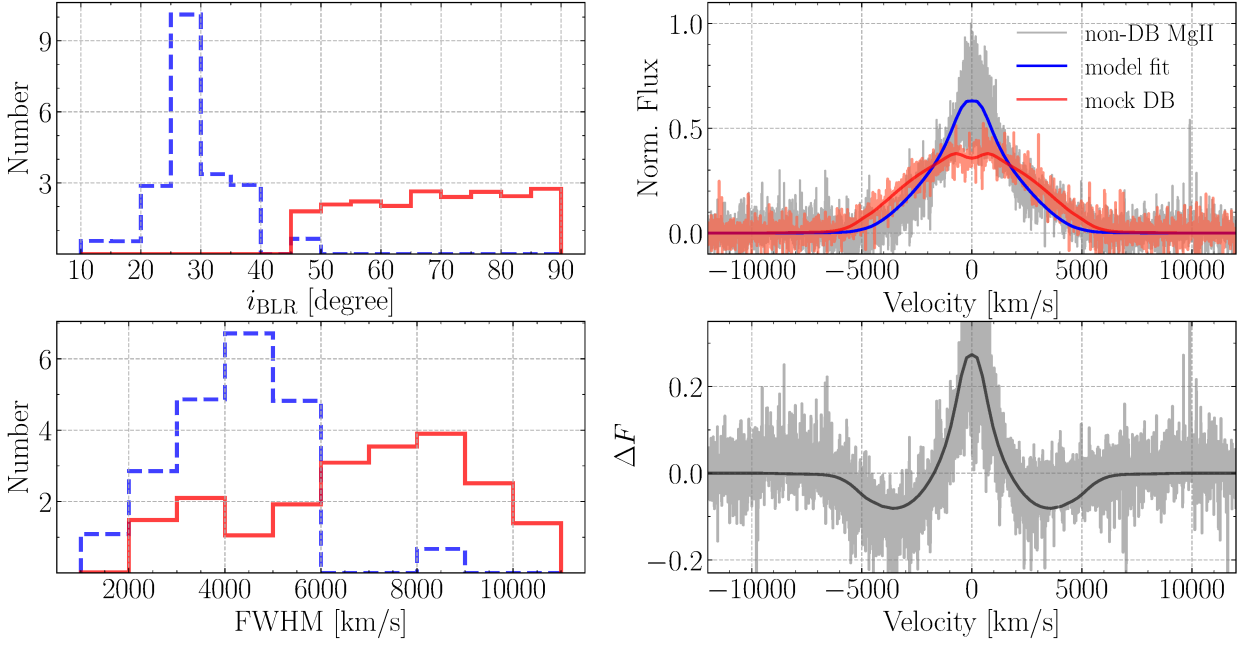


**Figure 4.** Expected stacked Mg II profile of the DB sample if those objects have flattened BLR geometry and are viewed with nearly edge-on orientations as suggested by the Doppler boost hypothesis to their periodicity. In the top-left panel, blue histogram represents the distribution of inclination angles for those 36 objects in the non-DB sample obtained from the simple BLR model fitting, and the red histogram represents the inclination angle distribution of 21 mock DB objects randomly selected over the range from  $\sin i = \sin 45^\circ$  to  $\sin 90^\circ$ . In the bottom-left panel, the blue histogram represents the FWHM distribution for those 36 objects in the non-DB sample, while the red histogram represents an FWHM distribution of the 21 objects in the mock DB sample randomly selected from the non-DB sample by replacing their inclination angles with those for the mock DB objects shown in the top-left panel (red histogram). The grey, blue, and red curves in the right panel show the stacked observed Mg II profile for the non-DB sample (same as the blue curve in the top-right panel of Fig. 3), the stacked modelled Mg II profile for the non-DB sample (blue curve; same as the black curve in the top-right panel of Fig. 3), and the expected stacked Mg II profile for the mock sample of 21 mock DB objects (red curve with the corresponding flux error, see Section 3 for details), respectively. The bottom-right panel shows the profile difference between the mock DB sample and the non-DB sample, the valleys and summit features shown here are significantly different from that shown in Fig. 2.

For a BBH system corotating in a circular orbit, the amplitude of the observed flux variability caused by the Doppler boost to the first order in  $v/c$  (Charisi et al. 2018) is:

$$A = (3 - \alpha_\nu) \frac{v}{c} \sin i_{\text{orb}}, \quad (4)$$

where  $v = \frac{1}{1+q} \left( 2\pi \frac{GM_{\bullet\bullet}}{P_{\text{orb}}} \right)^{1/3}$  is the orbital velocity,  $i_{\text{orb}}$  is the inclination angle of the orbital plane,  $q$  is the mass ratio. With the observed amplitude  $A_{\text{obs}}$  and  $\alpha_\nu$ , the orbital inclination angle is only determined by the orbital velocity  $v$ , i.e.,

$$\sin i_{\text{orb}} = \frac{A_{\text{obs}}}{3 - \alpha_\nu} \frac{c}{v} \quad (5)$$

Once the orbital period ( $P_{\text{orb}}$ ) and total mass ( $M_{\bullet\bullet}$ ) are given by observations, the orbital velocity  $v$  only varies with  $q$ . Since  $q$  ranges from 0 to 1, the maximum and minimum values of the orbital inclination angle can then be derived as

$$\sin i_{\text{orb}}^{\text{max}} = \frac{A_{\text{obs}}}{3 - \alpha_\nu} \frac{2c}{\left( 2\pi \frac{GM_{\bullet\bullet}}{P_{\text{orb}}} \right)^{1/3}} \quad (6)$$

$$\sin i_{\text{orb}}^{\text{min}} = \frac{A_{\text{obs}}}{3 - \alpha_\nu} \frac{c}{\left( 2\pi \frac{GM_{\bullet\bullet}}{P_{\text{orb}}} \right)^{1/3}} \quad (7)$$

After taking the observed  $A_{\text{obs}}$  and  $\alpha_\nu$  given in Table 2 of Charisi et al. (2018), the total mass  $M_{\bullet\bullet}$  and periods  $P_{\text{orb}}$  of the BBH systems given by Graham et al. (2015b) and Charisi et al. (2016), we can calculate  $\sin i_{\text{orb}}^{\text{min}}$  and  $\sin i_{\text{orb}}^{\text{max}}$  for each QSO in the DB sample. For the only one QSO in the DB sample (SDSS J154409.61+024040.0) that has  $\sin i_{\text{orb}}^{\text{min}} > 1$ , we simply set  $\sin i_{\text{orb}}^{\text{min}} = 1$  and  $\sin i_{\text{orb}}^{\text{max}} = 1$  for further analyses.

With the calculated  $i_{\text{orb}}^{\text{min}}$  and  $i_{\text{orb}}^{\text{max}}$ , we assume that  $i_{\text{orb}}$  is represented by the median value of  $[i_{\text{orb}}^{\text{min}}, i_{\text{orb}}^{\text{max}}]$  as

$$i_{\text{orb}} = \frac{i_{\text{orb}}^{\text{min}} + i_{\text{orb}}^{\text{max}}}{2}, \quad (8)$$

and the error of each  $i_{\text{orb}}$  is roughly

$$\sigma_i^{\text{orb}} = \frac{i_{\text{orb}}^{\text{max}} - i_{\text{orb}}^{\text{min}}}{2} \quad (9)$$

Figure 5 shows the distributions of inclination angles of the BBH orbital plane ( $i_{\text{orb}}$ ) and BLR ( $i_{\text{BLR}}$ ). In the DB sample, all the QSOs have  $i_{\text{BLR}} < 45^\circ$ , which are close to face on. The  $i_{\text{BLR}}$  distribution of the QSOs in the DB

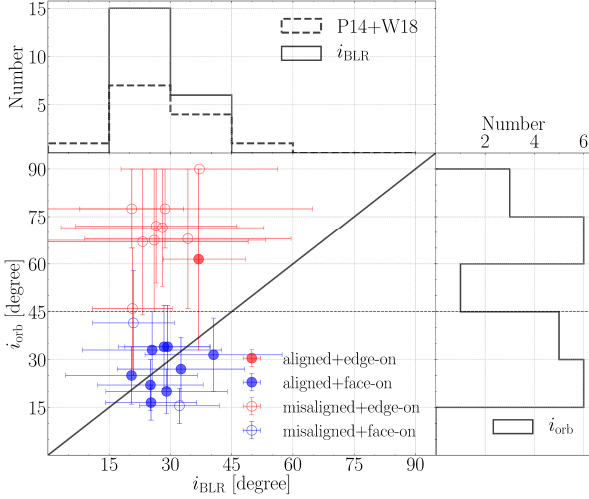


**Figure 5.** Distributions of  $i_{\text{orb}}$  and  $i_{\text{BLR}}$  for QSOs in the DB sample. The DB sample are classified into four subsamples, based on the alignment or misalignment of the orbital plane and BLR, and the viewing angle of SMBBH orbital plane, i.e., face-on or edge-on, of each QSO, i.e., 1) aligned and edge-on (red filled circles), 2) aligned and face-on (blue filled circles), 3) misaligned and edge-on (red open circles), and 4) misaligned and face-on (blue open circles). Top panel and right panel show the distributions of  $i_{\text{BLR}}$  (black histogram) and  $i_{\text{orb}}$  (black histogram) of the DB sample, respectively. In the top panel, we plot the  $i_{\text{BLR}}$  distribution with black histogram. For comparison, the dashed histogram presents the  $i_{\text{BLR}}$  distribution of normal QSOs (Pancoast et al. 2014b; Williams et al. 2018).

sample have no significant difference with that of those normal QSOs (top panel) given by Pancoast et al. (2014b) and Williams et al. (2018). Unlike the  $i_{\text{BLR}}$ , those orbital inclination angles  $i_{\text{orb}}$  show a bimodal distribution (right panel), which may suggest that not all the BBH orbital planes are aligned with their BLRs.

Based on the difference between the two inclination angles ( $\Delta i = i_{\text{orb}} - i_{\text{BLR}}$ ) and their corresponding errors, we find that 10 QSOs (filled circles in Figure 5) have  $i_{\text{orb}}$  and  $i_{\text{BLR}}$  roughly the same with each other, which indicates that their BBH orbital plane and the BLR are aligned. For the other 11 QSOs (open circles in Figure 5), their  $i_{\text{orb}}$  and  $i_{\text{BLR}}$  are significantly different from each other even after considering of their large uncertainties, which means that the BBH orbital planes in those systems are misaligned with the BLR planes.

According to the alignment or misalignment between the BBH orbital plane and BLR, and the face-on or edge-on view of BBH orbits, we further divide the DB sample into four subsamples: 1) 10 aligned systems (filled circles), 2) 11 misaligned systems (open circles), 3) 11 face-on orbital plane systems ( $i_{\text{orb}} \leq 45^\circ$ , blue circles), and 4) 10 edge-on orbital plane systems ( $i_{\text{orb}} > 45^\circ$ ). With these classifications, we then explore whether their stacked broad line profiles and FWHM distributions have different features.

Figure 6 shows the results of 10 aligned and 11 misaligned QSOs in the DB sample. Although the two kinds of QSOs have different  $\Delta i$  distribution (top-left panel), no

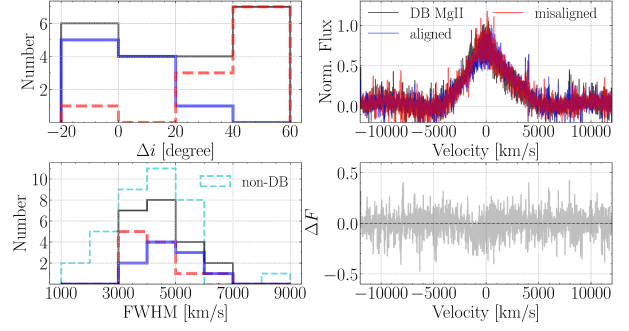


**Figure 6.** Stacked Mg II profiles and FWHM distributions of QSOs in the DB sample that are classified by the alignment and misalignment of  $i_{\text{orb}}$  and  $i_{\text{BLR}}$ . Top-left panel shows the inclination angle difference ( $\Delta i = i_{\text{orb}} - i_{\text{BLR}}$ ) of 10 aligned (blue histogram), 11 misaligned (red dashed histogram), and all the 21 (black histogram) QSOs in the DB sample. Bottom-left and top-right panels show the corresponding Mg II FWHM distributions and stacked profiles of the three subsamples labelled with colors the same as those in the top-left panel, respectively. For comparison, the FWHM distribution of the non-DB sample (cyan histogram) also shows in the bottom-left panel. Bottom-right panel shows the profile difference ( $\Delta F = F_{\text{aligned}} - F_{\text{misaligned}}$ ) between those two stacked profiles from the 10 aligned and 11 misaligned QSOs.

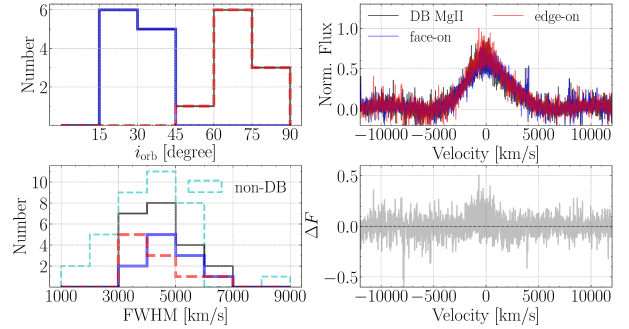


**Figure 7.** Stacked Mg II profiles and FWHM distributions of QSOs in the DB sample that are classified by the face-on and edge-on viewing angle  $i_{\text{orb}}$ . Top-left panel shows the orbital inclination angle  $i_{\text{orb}}$  distributions of 11 face-on (blue color), 10 edge-on (red color), and all the 21 (black color) QSOs in the DB sample. Bottom-left and top-right panels show the corresponding Mg II FWHM distributions and stacked profiles of the three subsamples labelled with colors the same as those in the top-left panel, respectively. For comparison, the FWHM distribution of the non-DB sample also shows in the bottom-left panel (cyan histogram). Bottom-right panel shows the profile difference ( $\Delta F = F_{\text{face-on}} - F_{\text{edge-on}}$ ) between those two stacked profiles from the 11 face-on and 10 edge-on QSOs.

significant difference appears for both the Mg II FWHM distributions (bottom-left panel) and stacked profiles (top-right panel). To check the detailed difference between the two stacked profiles, we show the flux residuals  $\Delta F = F_{\text{aligned}} - F_{\text{misaligned}}$  in the bottom-right panel, which fluctuate around zero and have no features like the valleys and summit that shown in Figure 4.

Figure 7 shows the Mg II FWHM distributions (bottom-

left panel) and the stacked Mg II line profiles (top-right panel) for those QSOs in the face-on and edge-on subsamples, respectively. Apparently there is no statistical difference between these two Mg II FWHM distributions, and the stacked Mg II profiles from the face-on and edge-on subsamples are quite similar with a flux residual in the velocity space close to zero as shown in the bottom-right panel.

Based on the above analyses, neither the aligned or misaligned nor the face-on or edge-on classifications of the DB sample present any distinguishable difference for both FWHM distributions and stacked Mg II broad lines. This conflicts with what we expect to the DB sample: the orbital orientations of these BBH systems distribute from face-on to edge-on, even though there is no correlations between  $i_{\text{orb}}$  and  $i_{\text{BLR}}$ , we should still have opportunities to observe the BLR in edge-on like inclination angles for a DB sample with 21 QSOs. Current results support that we can observe those BBH orbits in both edge-on and face-on, but all of them only have face-on oriented BLRs, which further enhance the challenge for using the Doppler boost hypothesis to interpret the QSOs with optical periodicity in the DB sample.

#### 4 CONCLUSIONS

Optical periodicity QSOs are proposed to be candidates of the sub-parsec BBHs. The periodic variations of a number of these candidates were suggested to be due to orbital modulated Doppler boosted continuum radiation from the secondary component of the BBH systems if viewing with close to edge-on orientations (D’Orazio et al. 2015; Charisi et al. 2018). With this relativistic Doppler boost hypothesis, Charisi et al. (2018) further divided these BBH candidates into two classes according to their spectral properties, i.e., one class that can be explained by the Doppler boost (DB) effect (DB objects) and the other class that cannot (non-DB objects).

In this paper, we investigate the properties of the broad emission lines of both the proposed DB and non-DB objects by using their SDSS spectra and further test the DB hypothesis. We find that the properties of various broad emission lines of the DB objects are similar to those of the non-DB objects and the stacked C IV, C III], and Mg II line profiles of the DB sample are almost the same as those of the non-DB sample. Under the DB hypothesis, however, we demonstrate that the stacked broad lines of the DB sample, such as C IV, C III], Mg II are expected to be double-peaked and significantly broader than those of the non-DB sample, by reasonably assuming that the DB objects have similar flattened BLR geometry and structures as that of the non-DB objects but viewing preferentially at close to edge-on orientation under the DB hypothesis. This expectation is in contradiction with the observational results of no difference between the stacked broad emission line profiles of the proposed DB and non-DB samples, which raises a significant challenge to the Doppler boost interpretation for some of those BBHs candidates suggested by their optical periodicity.

By deriving the inclination angles of BLRs ( $i_{\text{BLR}}$ ) from the MCMC fittings of the QSO broad lines by a simple BLR model and estimating the orbital inclination angles ( $i_{\text{orb}}$ ) of the SMBBH orbital planes based on the DB hypothesis, we

find that all the BLRs of QSOs in the DB sample are viewed from face-on orientations, while the BBH orbits viewed in the face-on and edge-on orientations are half-to-half. For the 21 QSOs in the DB sample, 10 of them may have the BLRs aligned with the BBH orbital planes, while the others are not. However, after comparing the FWHM distributions and stacked Mg II profiles of these subsamples, no significant differences are found either between those obtained from the face-on and edge-on subsamples or between those from the aligned and misaligned subsamples. This further enhances the challenge on using Doppler boost hypothesis to interpret the optical periodicity of the systems in the DB sample. Even if the inclination angles of the BBH orbital planes are not correlated with the BLRs, it is still surprising that no single BLR is viewed at edge-on orientation, while both face-on and edge-on orientations of the BBH orbital planes are found in the DB sample with 21 QSOs.

#### ACKNOWLEDGEMENTS

This work is supported by the National Key Program for Science and Technology Research and Development (Grant No. 2016YFA0400704), the National Natural Science Foundation of China (NSFC) under grant number 11690024 and 11873056, and the Strategic Priority Program of the Chinese Academy of Sciences (Grant No. XDB 23040100).

#### REFERENCES

- Albareti, F. D., Allende Prieto, C., Almeida, A., et al. 2017, *ApJS*, 233, 25
- Antonucci, R. 1993, *ARA&A*, 31, 473
- Begelman, M. C., Blandford, R. D., & Rees, M. J. 1980, *Nature*, 287, 307
- Bentz, M. C., Denney, K. D., Grier, C. J., et al. 2013, *ApJ*, 767, 149
- Blumenthal, G. R., & Mathews, W. G. 1975, *Lick Observatory Bulletin*, 689, 1
- Blumenthal, G. R., & Mathews, W. G. 1976, *ApJ*, 203, 714
- Charisi, M., Bartos, I., Haiman, Z., et al. 2016, *MNRAS*, 463, 2145
- Charisi, M., Haiman, Z., Schiminovich, D., & D’Orazio, D. J. 2018, *MNRAS*, 476, 4617
- D’Orazio, D. J., Haiman, Z., & Schiminovich, D. 2015, *Nature*, 525, 351
- Eracleous, M., Boroson, T. A., Halpern, J. P., & Liu, J. 2012, *ApJS*, 201, 23
- Foreman-Mackey, D., Hogg, D. W., Lang, D., et al. 2013, *PASP*, 125, 306
- Graham, M. J., Djorgovski, S. G., Stern, D., et al. 2015a, *Nature*, 518, 74
- Graham, M. J., Djorgovski, S. G., Stern, D., et al. 2015b, *MNRAS*, 453, 1562
- Gravity Collaboration, Sturm, E., Dexter, J., et al. 2018, *Nature*, 563, 657
- Guo, H., Liu, X., Shen, Y., et al. 2019, *MNRAS*, 482, 3288
- Ju, W., Greene, J. E., Rafikov, R. R., Bickerton, S. J., Badenes, C. 2013, *ApJ*, 777, 44
- Kaspi, S., Smith, P. S., Netzer, H., et al. 2000, *ApJ*, 533, 631
- Kaspi, S., Brandt, W. N., Maoz, D., et al. 2007, *ApJ*, 659, 997
- Kormendy, J., & Ho, L. C. 2013, *ARA&A*, 51, 511
- Krolik, J. H. 2001, *ApJ*, 551, 72



- Krolik, J. H. 1999, Active galactic nuclei : from the central black hole to the galactic environment / Julian H. Krolik. Princeton, N. J. : Princeton University Press, c1999.,
- Li, Y.-R., Wang, J.-M., Zhang, Z.-X., et al. 2019, ApJS, 241, 33
- Liu, X., Shen, Y., Bian, F., Loeb, A., & Tremaine, S. 2014, ApJ, 789, 140
- Liu, T., Gezari, S., Ayers, M., et al. 2019, ApJ, 884, 36
- Lu, K.-X., Li, Y.-R., Bi, S.-L., & Wang, J.-M. 2016, MNRAS, 459, L124
- Magorrian, J., Tremaine, S., Richstone, D., et al. 1998, AJ, 115, 2285
- Pancoast, A., Brewer, B. J., Treu, T., et al. 2012, ApJ, 754, 49
- Pancoast, A., Brewer, B. J., & Treu, T. 2014a, MNRAS, 445, 3055
- Pancoast, A., Brewer, B. J., Treu, T., et al. 2014b, MNRAS, 445, 3073
- Peterson, B. M. 1997, An introduction to active galactic nuclei, Publisher: Cambridge, New York Cambridge University Press, 1997 Physical description xvi, 238 p. ISBN 0521473489,
- Sigut, T. A. A., & Pradhan, A. K. 2003, ApJS, 145, 15
- Sigut, T. A. A., Pradhan, A. K., & Nahar, S. N. 2004, ApJ, 611, 81
- Tremaine, S., Gebhardt, K., Bender, R., et al. 2002, ApJ, 574, 740
- Tsalmantza, P., Decarli, R., Dotti, M., & Hogg, D. W. 2011, ApJ, 738, 20
- Williams, P. R., Pancoast, A., Treu, T., et al. 2018, ApJ, 866, 75
- Xin, C., Charisi, M., Haiman, Z., et al. 2019, arXiv e-prints, arXiv:1907.11246
- Yan, C.-S., Lu, Y., Dai, X., & Yu, Q. 2015, ApJ, 809, 117
- Yu, Q. 2002, MNRAS, 331, 935
- Zheng, Z.-Y., Butler, N. R., Shen, Y., et al. 2016, ApJ, 827, 56